



Toledo, D., Irwin, P. G. J., Teanby, N. A., Simon, A. A., Wong, M. H., & Orton, G. S. (2018). Uranus's Northern Polar Cap in 2014. *Geophysical Research Letters*, 45(11), 5329-5335. <https://doi.org/10.1029/2018GL077654>

Peer reviewed version

Link to published version (if available):
[10.1029/2018GL077654](https://doi.org/10.1029/2018GL077654)

[Link to publication record in Explore Bristol Research](#)
PDF-document

This is the author accepted manuscript (AAM). The final published version (version of record) is available online via Wiley at <https://agupubs.onlinelibrary.wiley.com/doi/abs/10.1029/2018GL077654> . Please refer to any applicable terms of use of the publisher.

University of Bristol - Explore Bristol Research

General rights

This document is made available in accordance with publisher policies. Please cite only the published version using the reference above. Full terms of use are available:
<http://www.bristol.ac.uk/pure/about/ebr-terms>

Uranus's northern polar cap in 2014

Daniel Toledo¹, Patrick G. J. Irwin¹, Nicholas A. Teanby², Amy A. Simon³, Michael H. Wong⁴ and Glenn S. Orton⁵

¹Department of Physics (Atmospheric, Oceanic and Planetary Physics), University of Oxford, Parks Rd, Oxford OX1 3PU, UK.

²School of Earth Sciences, University of Bristol, Wills Memorial Building, Queens Road, Bristol, BS8 1RJ, UK.

³NASA Goddard Space Flight Center Solar System Exploration Division (690) Greenbelt, MD 20771, USA.

⁴University of California at Berkeley Astronomy Department Berkeley, CA 94720-3411, USA.

⁵Jet Propulsion Laboratory, California Institute of Technology, 4800 Oak Grove Drive, Pasadena, CA 91109, USA.

Corresponding author: Daniel Toledo (daniel.toledocarrasco@physics.ox.ac.uk)

Key Points:

- Aerosols, dynamics, Equinox

19 **Abstract**

20 In October and November 2014, spectra covering the 1.436 – 1.863- μm wavelength range
21 from the SINFONI Integral Field Unit Spectrometer on the Very Large Telescope showed the
22 presence of a vast bright North polar cap on Uranus, extending northward from about 40°N and
23 at all longitudes observed. The feature, first detected in August 2014 from Keck telescope
24 images, has a morphology very similar to the southern polar cap that was seen to fade before the
25 2007 equinox. At strong methane-absorbing wavelengths (for which only the high troposphere or
26 stratosphere is sampled) the feature is not visible, indicating that it is not a stratospheric
27 phenomenon. We show that the observed northern bright polar cap results mainly from a
28 decrease in the tropospheric methane mixing ratio, rather than from a possible latitudinal
29 variation of the optical properties or abundance of aerosol, implying an increase in polar
30 downwelling near the tropopause level.

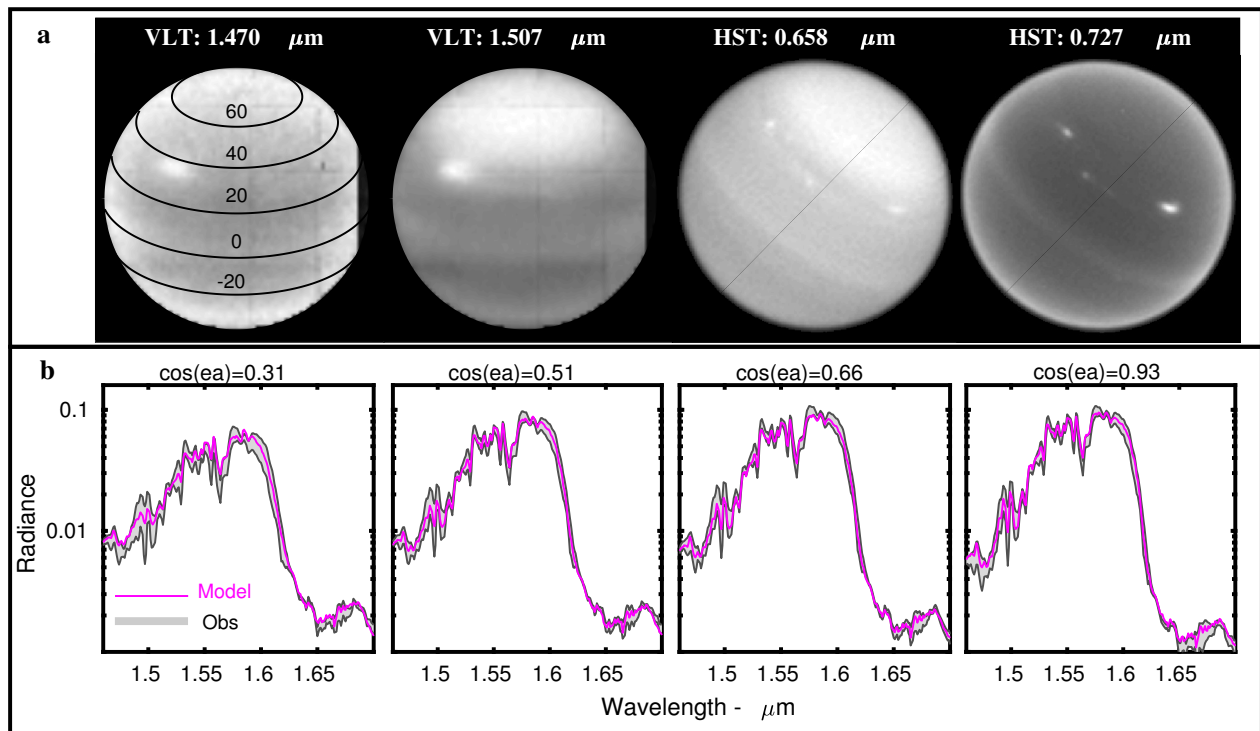
31 **1 Background**

32 Uranus undergoes a cycle of dramatic seasonal atmospheric changes in cloud and hazes,
33 driven by its extremely large obliquity (98°). Different observations have revealed, for instance,
34 the presence of discrete clouds and convective systems at different locations and time periods
35 (e.g. Irwin et al., 2017; de Pater et al., 2015; Sromovsky & Fry, 2007), or the formation and
36 dissipation of bright polar regions in both hemispheres before and after the 2007 equinox (e.g.
37 Hofstadter & Butler, 2003; Irwin et al., 2016; Irwin, Teanby, et al., 2012; Karkoschka, 2001;
38 Karkoschka & Tomasko, 2009; Rages et al., 2004; Sromovsky & Fry, 2007). Voyager
39 observations of Uranus in 1986 recorded for the first time the presence of a bright south polar
40 cap extending southward from about 45°S. Although observations made between 1994-2003
41 showed temporal variations in brightness in the south polar region, they did not record signs of a
42 northern polar cap with comparable brightness to that observed in the south pole (Hammel &
43 Lockwood, 2007; Rages et al., 2004). Near equinox in 2007, however, Uranus' atmosphere
44 underwent a number of seasonal changes that led to a reversal in the polar brightness: a south
45 polar collar at 45°S diminishing in brightness relative to mid-latitudes, and a north polar collar at
46 45°N becoming steadily brighter with time (Irwin, Teanby, et al., 2012). In August 2014, a large
47 bright polar-cap-like feature was identified in Uranus's northern pole from Keck telescope
48 images (de Pater et al., 2015), whose progressive formation over 2013 was observed by amateur
49 telescopes (see PVOL database, Hueso et al., 2018). Based on long-term records of Uranus
50 brightness variations before the 2007 equinox (Hammel & Lockwood, 2007; Lockwood &
51 Jerzykiewicz, 2006), it was thought that the polar cap could be a seasonal formation or re-
52 distribution of aerosols (de Pater et al., 2015; Sromovsky et al., 2015).

53 Observations of Uranus in October and November 2014 with the Wide Field Camera 3
54 (WFC3) instrument of the Hubble Space Telescope (HST) and the SINFONI Integral Field Unit
55 Spectrometer on the Very Large Telescope (VLT) confirmed the presence of the ubiquitous
56 bright cap from 40° to 90°N (**Figure 1a**) (Irwin et al., 2017). The feature does not appear at 1.47
57 and 0.727- μm methane-absorbing wavelengths, where the fraction of radiance transmitted to
58 space is less than 0.5 for pressures greater than ~ 0.1 bar, the pressure of the tropopause. This
59 indicates that if the polar cap is the result of variations in aerosol distribution, these variations
60 must occur at altitudes below the tropopause. This result was also tested using the cloud
61 properties and methane concentration obtained at polar cap latitudes (see section 3.2). The
62 purpose of this work is to determine the nature of Uranus's polar cap in 2014. To this end, we
63 analyzed spectra covering the 1.46-1.70- μm wavelength range of the VLT/SINFONI

64 observations taken in 2014, which provide a clear mapping of the feature at both high spatial and
 65 spectral resolution.

66



67

68 **Figure 1.** (a) VLT and HST images at 1.470, 1.507, 0.658 and 0.727 μm made on 31st October
 69 and 9th November 2014, respectively. The polar cap can be identified at 1.507 and 0.658 μm for
 70 latitudes higher than 40°N . (b) Comparisons between radiative-transfer model and observations
 71 at 32°N . The thick grey solid lines represents VLT spectra with errors at 32°N (far away from the
 72 polar cap) with emission angles (ea) of 72° , 59° , 49° and 22° respectively ($\cos(\text{ea})=0.31$, 0.51,
 73 0.66 and 0.93). These observations were selected at longitudes away from the storm system
 74 observed in VLT and HST images (Irwin et al., 2016; Irwin et al., 2017). The shaded errors
 75 represent the random errors of the observed radiances and are computed by the VLT/SINFONI
 76 pipeline. The four spectra were fitted simultaneously using the 3-cloud model discussed in
 77 section 3 (purple dashed lines) whose reduced chi-squared value was found to be 0.77.

78 2 Observations, cloud model and radiative transfer analysis

79 We analyzed observations of Uranus performed by the SINFONI instrument on October 31st
 80 and November 11th, 2014, at the European Southern Observatory (ESO) Very Large Telescope
 81 (VLT) in Paranal, Chile. SINFONI is an Integral Field spectrograph that can make use of
 82 adaptive optics to yield a spatial resolution of about $0.1''$ and returns 64×64 -pixel spectral cubes,
 83 where each “spaxel” has 2048 wavelengths. SINFONI has three spaxel scale settings: $0.25''$, $0.1''$
 84 and $0.025''$ resulting in fields of views (FOV) of $8'' \times 8''$, $3'' \times 3''$ and $0.8'' \times 0.8''$, respectively.
 85 Uranus was imaged with the $0.1''$ pixel scale and the H-grism, which has a spectral resolution of
 86 $0.0005 \mu\text{m}$ and covers the wavelength range $1.436 - 1.863 \mu\text{m}$. The data were first reduced with
 87 the ESO VLT SINFONI pipeline, with additional photometric corrections as described by Irwin

88 et al. (2016), and then averaged with a triangular-shaped instrument function with Full Width
89 Half Maximum (FWHM) = 0.002 μm , resulting in a final spectral resolution of $R \sim 775$. It was
90 found in previous analyses of Uranus that this spectral resolution provides the best compromise
91 between modelling computational speed, signal-to-noise (SNR) ratio and accurate representation
92 of the methane absorption features (Irwin et al., 2012).

93 The NEMESIS correlated-k radiative-transfer and retrieval code (Irwin et al., 2008) was
94 used to simulate the absorption and scattering of Uranus's atmosphere. The methane absorption
95 was calculated using the WKMC-80K line database (Campargue et al., 2012) and assuming the
96 'F1' temperature profile of Sromovsky et al., (2011) which has a He:H₂ ratio of 0.131 and
97 assumes a 0.04% mole fraction of neon and a deep CH₄ mole fraction of 4% at non-polar
98 latitudes (Karkoschka & Tomasko, 2009). Although the temperature profile may change at polar
99 latitudes, these changes are not expected to cause an impact in our retrievals since the thermal
100 structure of Uranus is not strongly variable. We tested what is the effect of adding a random
101 noise with different amplitudes to the F1 profile, and we found that the retrieved aerosol
102 parameters do not differ significantly. Figure S1 in the supporting information provides more
103 detail on these tests. The line data were converted to k-distribution look-up tables, covering the
104 VLT spectral range and assuming a triangular-shaped instrument function with FWHM = 0.002
105 μm . Collision induced absorptions by H₂-H₂ and H₂-He collision-induced (CIA) were computed
106 using the coefficients of Borysow et al., (1989, 2000) and Zheng & Borysow (1995) and an
107 equilibrium ortho/para-H₂ ratio was assumed at all altitudes and locations. Absorption by H₂-
108 CH₄ and CH₄-CH₄ collision-induced was also computed (Borysow & Frommhold, 1987).
109 Although the assumption of equilibrium ortho/para-H₂ may not valid for all the latitudes, we
110 emphasize that for our wavelength range this parameter does not have an impact on the
111 retrievals.

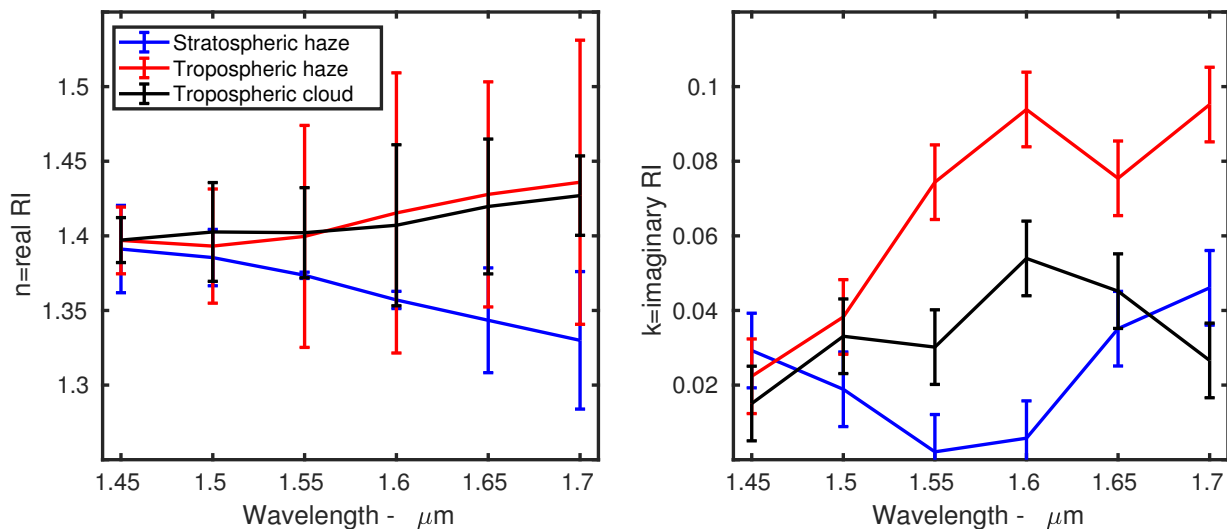
112 **3 Analysis procedure and results**

113 **3.1 Analysis at latitudes < 40°N**

114 To determine the nature of the polar cap, we first conducted a number of limb-darkening
115 analyses of the VLT/SINFONI spectra (covering the 1.46-1.70- μm wavelength range) at latitudes
116 away from the polar cap. For each latitude selected, four spectra taken at different emission
117 angles (ranging from 20° to 75°) were fitted simultaneously using a three-layer cloud model
118 comprising a thick tropospheric cloud based near the 2-bar pressure level and two vertically
119 extended haze layers with bases in the troposphere (~ 0.56 bar) and near the tropopause (~ 0.19
120 bar); the first two pressure levels were selected based on previous analyses of clouds and haze
121 (Irwin et al., 2016; Irwin et al., 2017; Sromovsky et al., 2011). The main difference of this model
122 compared with the two-layer cloud model used in previous analyses (Irwin et al., 2016; Irwin et
123 al., 2015; Irwin et al., 2017) is the addition of a stratospheric haze layer, which was required for
124 fitting VLT spectra observed over a wide range of emission angles simultaneously. The vertical
125 distribution of each cloud layer is characterized by the total opacity at 1.4 μm (τ), the fractional
126 scale height (FSH) and the cloud base altitude (h), parameters that can be retrieved or kept fixed
127 in the analysis. The aerosol scattering properties (single-scattering albedo, phase function and
128 extinction cross-section) are computed at all wavelengths using Mie theory, with the phase
129 functions approximated with Henyey-Greenstein functions to average over the characteristic
130 'glory' and 'rainbow' of spherical particles. To calculate these properties, the parameters
131 required (that can be retrieved or kept fixed) are the size distribution of the aerosol particles, the

132 imaginary refractive index spectrum (assumed to be the same at all vertical levels), and the real
 133 part of the refractive index at a single wavelength; the real part of the refractive index at all other
 134 wavelengths is calculated using the Kramers-Kronig relation (e.g. Sheik-Bahae 2015).

135 The bases of the three layers were fixed in the model, while the fractional scale height was
 136 retrieved for the two haze layers, but fixed for the tropospheric cloud to a value of 0.01 (Irwin et
 137 al., 2016), to make it vertically thin. For the radiative-transfer simulations, the atmosphere was
 138 split into 39 levels equally spaced in log pressure between 12 bar and 0.003 bar. The total
 139 opacity, particle effective radius (assuming a standard Gamma distribution) and the imaginary
 140 part of the refractive index spectrum of each of the three cloud layers were retrieved. The real
 141 refractive index spectrum was derived using the Kramers-Kronig analysis assuming a real
 142 refractive index of 1.4 at a wavelength of 1.6 μm , and the spectrum of the imaginary refractive
 143 index was retrieved at 6 wavelengths assuming a certain correlation in order to retrieve a smooth
 144 spectrum (and so to avoid unrealistic variations). We find that effective radii of $\sim 1 \mu\text{m}$ for the
 145 tropospheric cloud, and of ~ 0.8 and $0.05 \mu\text{m}$, respectively, for the tropospheric and stratospheric
 146 haze layers provide the best results in the limb-darkening analyses performed at different non-
 147 polar latitudes. This model was able to achieve fits with reduced chi-squared (χ^2_{red}) values
 148 smaller than 1. **Figure 1b** shows, as an example, a limb darkening analysis carried out at 32°N
 149 with the three-cloud model and whose retrieved refractive index is illustrated in **Figure 2**.
 150 Similar limb-darkening analyses performed at different latitudes showed that the imaginary
 151 refractive index spectrum (and derived real part) and size distribution of each cloud layer are
 152 very similar at all the locations. Therefore, for the analysis of the cloud and haze at polar
 153 latitudes we use the refractive index and size distribution derived in this section as reference.



154

155 **Figure 2.** Fitted refractive index (RI) spectra from the limb-darkening observations using
 156 NEMESIS for the three cloud layers. Left panel shows the real RI and right panel the imaginary
 157 RI. Data at 32°N (outside the polar region) were used to constrain RI, but results for other
 158 latitudes were highly consistent with these values.

159 3.2 Analysis at polar-cap latitudes

160 The same 3-cloud model was used at latitudes lying within the polar ‘cap’, but assuming
 161 different values of the deep methane mixing ratio: 1.5, 2, 2.5, 3, 3.5 and 4%. This selection of

162 values is based on previous analyses that found a depletion of methane at polar latitudes (Irwin,
 163 Teanby, et al., 2012; Karkoschka & Tomasko, 2009; de Kleer et al., 2015; Sromovsky et al.,
 164 2011, 2014; Tice et al., 2013). For different polar latitudes, we fitted four spectra taken at
 165 different emission angles (whose range of values depends on the latitude) for these different
 166 methane concentrations and using the refractive index and size distribution derived in previous
 167 section (latitudes <40°N). Although this 3-cloud model is able to achieve fits with χ^2_{red} values <1
 168 at polar latitudes, we found a strong correlation between the tropospheric cloud altitude and the
 169 methane concentration. This correlation results from the fact that the absorption of light by
 170 methane above the cloud deck is reduced as the cloud altitude increases. Therefore, an
 171 overestimation of the deep methane volume mixing ratio (CH₄ VMR) in the pole can occur if the
 172 retrieved tropospheric cloud altitude (h_{tc}) is higher at these latitudes. In order to study the
 173 possible combinations of solutions we carried out a number of limb-darkening analyses for a set
 174 of cloud altitudes (-24, -22, -20, -18, -16, -14 and -12 km, or in pressure units 2, 1.89, 1.78, 1.68,
 175 1.58, 1.47 and 1.22 bars, respectively) and deep methane volume mixing ratios (0.015, 0.020,
 176 0.025, 0.030, 0.035 and 0.040). For each h_{tc} -CH₄ VMR combination, we retrieved the opacity of
 177 the three cloud layers and the FSH of the two haze layers by fitting four spectra taken at different
 178 emission angles. These limb-darkening analyses were conducted at latitudes within and near the
 179 polar cap edge. The upper panels of **Figure 3** show contour plots of χ^2_{red} in the h_{tc} -CH₄ VMR
 180 space for limb-darkening analyses performed at 38°, 42°, 55° and 70°N, while the lower panels
 181 show the contour plots of the retrieved tropospheric cloud opacity (τ_{tc}). Note that limb-darkening
 182 analyses at higher latitudes were not performed due to the limited range of emission angles at
 183 such latitudes. For example the emission angles of the observations at 38°N were found to lie
 184 between 17°-73° while at 70°N between 43°-73°. We tested that this change in the emission-
 185 angle range between the different latitudes does not have a major impact on our retrievals (see
 186 figure S2 in the supporting information for more details).

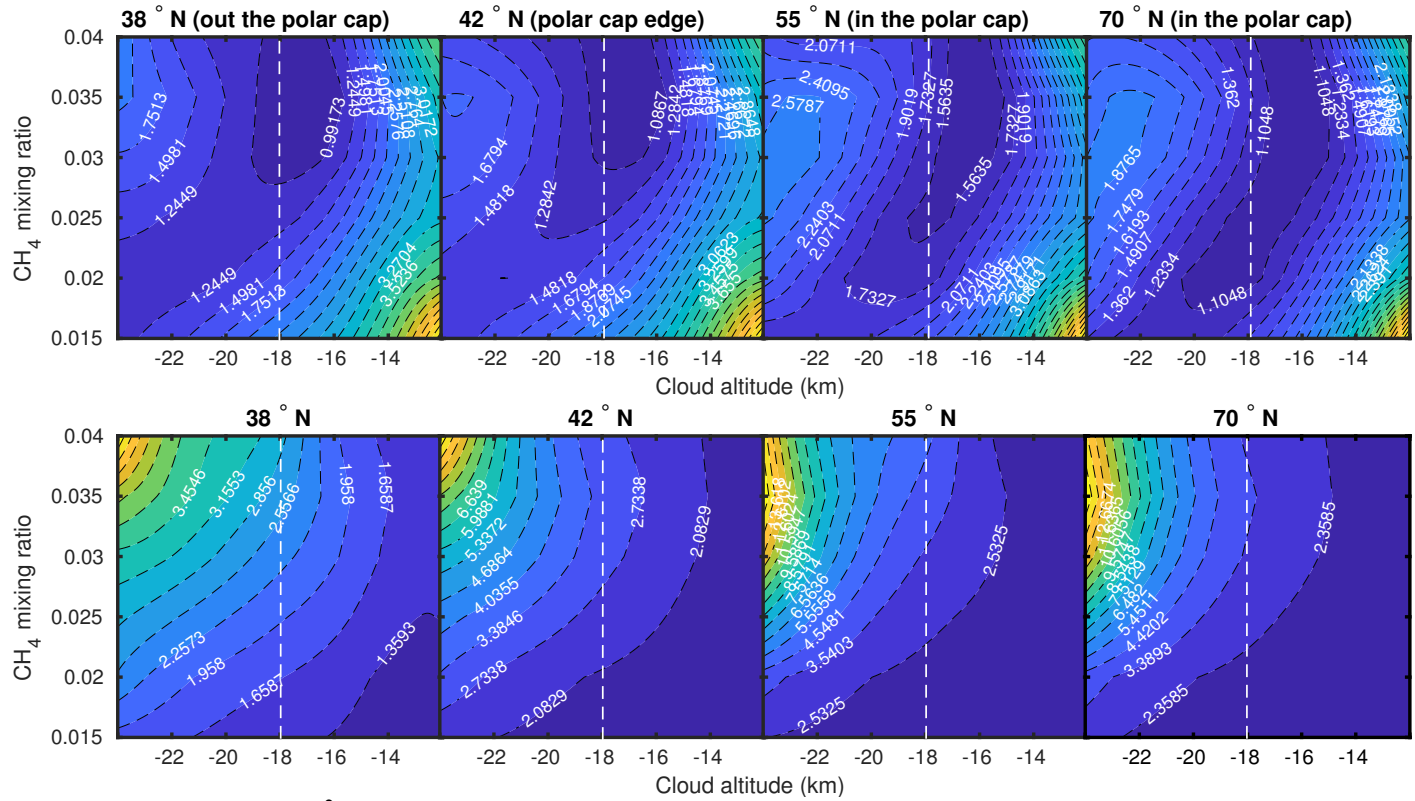
187 We observe that at 38° and 42°N (far-from and near-to the polar cap edge) the minimum
 188 values of χ^2_{red} are found for CH₄ VMRs greater than 0.03, while at 55° and 70°N (within the
 189 polar cap) the best solutions are given for values between 0.02 and 0.04. Sromovsky et al.,
 190 (2014) found CH₄ concentrations smaller than 0.03 at latitudes polewards of 40°N and of ~
 191 0.035-0.04 for the rest of non-polar latitudes in 2012, using wavelength ranges with
 192 complementary hydrogen and methane absorption. Assuming a similar distribution of methane in
 193 2014, the lower panels of **Figure 3** show a retrieved opacity at 1.4 μm of the tropospheric cloud
 194 of 2.5 ± 0.4 at 38°N and 2.8 ± 0.4 at 70°N. In order to examine the main polar cap signatures in the
 195 VLT spectra and to study whether such an increase in the tropospheric cloud opacity can cause
 196 the change in brightness seen in both VLT and HST images (see **Figure 1a**), we took the
 197 difference between spectra at the 26° and 46°N locations (**Figure 4a**). These signatures can be
 198 compared with those observed when changing some of the parameters of the model, such as the
 199 tropospheric cloud opacity or the CH₄ VMR. We found that the polar cap signature illustrated in
 200 **Figure 4a** does not correlate well with the variation obtained in the simulated 46°N spectrum
 201 when the tropospheric cloud opacity is increased from 2.5 to 3 or from 2.5 to 3.5. Note also that
 202 results illustrated in **Figure 3** show tropospheric cloud opacity differences between polar and
 203 non-polar latitudes of only ~0.5 (close to our formal uncertainty $\Delta\tau_{\text{tc}}=0.4$). Therefore, these
 204 results indicate that the mean features of the polar cap are not the result of a significant variation
 205 of the tropospheric cloud opacity. Similar conclusions are derived for the tropospheric haze for
 206 which we found opacities of 0.049 ± 0.001 and 0.0395 ± 0.0015 at 38 and 70°N, respectively (i.e. a
 207 slight decrease in the polar latitudes). Regarding the stratospheric haze, we found opacities of

208 0.242±0.003 and 0.263±0.004 at 38 and 70°N, respectively. This 10% increase in stratospheric
209 haze opacity near the pole is a statistically significant difference, but it cannot be the cause of the
210 prominent polar cap because the polar brightening is seen only at wavelengths probing deeper
211 than the tropopause (Sec. 1).

212 These results show that the polar cap observed in VLT images cannot be explained by an
213 accumulation of aerosol; neither by variations in the cloud/haze scattering properties since the
214 same refractive indices and size distributions derived in section 3.1 at 32°N were used and found
215 to provide a good fit. The observed timescales for the formation of the polar cap discards a
216 possible haze accumulation due to changes in haze mass production rate over the solar cycle
217 after 2007 equinox. Indeed, the response of the haze to changes in its production rate is much too
218 sluggish (Pollack et al., 1987) to explain the polar cap formation. Thus, this indicates that
219 dynamics may be important on the formation of the polar cap through variations in the
220 atmospheric circulation before and after 2007 equinox. These variations in the atmospheric
221 circulation would lead to a redistribution of the haze (particle size and column mass) by
222 transporting small particles from upwelling regions to the North pole. Although this transport of
223 small haze particles to the polar region could play a role in the polar cap formation, their small
224 cross section at near-IR wavelengths (small optical depth) may explain why our limb-darkening
225 analyses do not show a noticeable latitudinal variation in the aerosol properties.

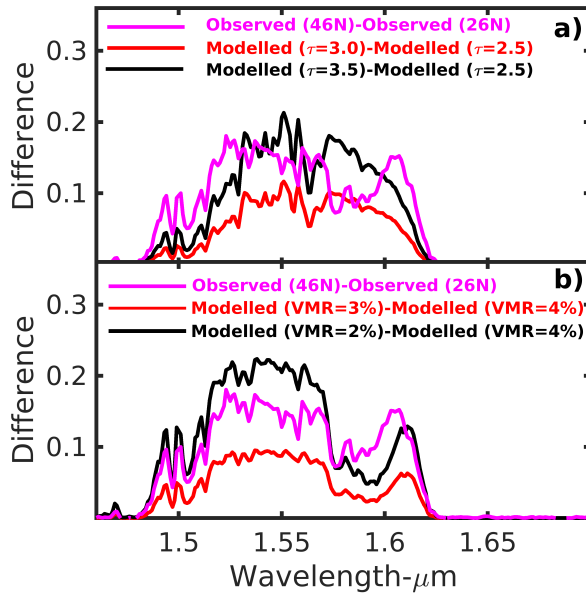
226 Results illustrated in the upper panels of **Figure 3** show that the observations in the polar
227 cap and near the polar cap edge (determined by the change in brightness in VLT and HST
228 images) can be fitted using a lower CH₄ concentration and a similar tropospheric cloud altitude
229 to that found at non-polar latitudes. We found also that the polar cap signature illustrated in
230 **Figure 4a** correlates well with the variation obtained in the simulated 46°N spectrum when the
231 methane mixing ratio is modified from 4 to 2% or from 4 to 3% (**Figure 4b**). Since these mixing
232 ratios correspond to the values found at latitudes outside and within the polar ‘cap’, the results
233 shown in **Figures 4b** suggest that the strong contrast observed between the polar ‘cap’ and lower
234 latitudes is mainly the result of the depletion of methane. Note that at polar latitudes methane
235 mixing ratios between 2 and 4% (**Figure 3**) can provide good fits because the altitude of the
236 tropospheric cloud is a free parameter as well. Since the absorption of light by methane increases
237 as the cloud altitude decreases, similar signatures as illustrated in **Figures 4b** can be produced by
238 increasing the cloud altitude in the model. However, the possibility of an increase of the
239 brightness as a result of an increase in the cloud altitude (instead of from a decrease in the
240 methane mixing ratio) is not consistent with the observed tropospheric methane depletion at
241 pressure levels not greater than ~ 3 bar at polar latitudes (Sromovsky et al., 2014).

242



243
 244
 245
 246
 247
 248
 249

Figure 3. Contours of χ^2_{red} (upper panels) in the $h_{\text{ic}}\text{-CH}_4$ VMR space obtained from a number of limb-darkening analyses performed at 38° , 42° , 55° and 70°N . Lower panels show contours of the tropospheric cloud opacity retrieved from these analyses. The altitudes -24, -22, -20, -18, -16, -14 and -12 km correspond to the pressure levels 2, 1.89, 1.78, 1.68, 1.58, 1.47 and 1.22 bar, respectively.



250

251 **Figure 4.** (a) Differences between observed spectra at 46° and 26°N (ea~20°) showing the polar
 252 ‘cap’ spectral signature in the VLT spectra (purple solid line), and variations in the simulated
 253 46°N spectrum when the tropospheric cloud opacity is changed from 2.5 to 3 (red solid line) and
 254 from 2.5 to 3.5 (black solid line). (b) Differences between observed spectra at 46° and 26°N
 255 (ea~20°) showing the polar ‘cap’ spectral signature in the VLT spectra (purple solid line), and
 256 variations in the simulated 46°N spectrum when the CH₄ mixing ratio is changed from 4 to 3%
 257 (red solid line) and from 4 to 2% (black solid line). The comparison in panel b shows that the
 258 main polar cap spectral signature is similar to that obtained when the methane mixing ratio is
 259 varied from the value found at polar latitudes to that at latitudes far away from the feature.

260 4 Conclusions

261 The bright polar cap observed by VLT/SINFONI and HST/WFC3 in 2014 is mainly due to
 262 the decrease in the methane concentration at polar latitudes. By observing the brightness spatial
 263 variations, the VLT observations show the presence of the polar cap at latitudes 40° to 90°N,
 264 indicating a hole-like depletion of methane. This methane latitudinal distribution supports
 265 scenarios consisting of an upwelling of methane gas at low latitudes, a condensation of methane
 266 in the cooler troposphere, and a descent of the now dried-out gas back to the deep atmosphere at
 267 high latitudes (Karkoschka & Tomasko, 2009; Sromovsky et al., 2011). The temporal variation
 268 of the latitudinal distribution of methane depletion can result from latitudinal variations in the
 269 gas upwelling rates, which in turn may be due to a Hadley overturning circulation or to a
 270 latitudinal variation in the rate of vertical eddy mixing. However, for clarifying which processes
 271 are involved in the formation and stability of the northern polar cap we require coupled
 272 dynamics-microphysics simulations of Uranus' atmosphere. These coupled simulations will
 273 clarify the role played by methane clouds in the polar methane depletion, and therefore in the
 274 polar cap formation.

275 Acknowledgments

276 The VLT/SINFONI observations were performed at the European Southern Observatory
 277 (ESO), Proposal 092.C-0187. The HST observations were made with the NASA/ESA Hubble

278 Space Telescope under programs GO13937/14334. Support for this latter program was provided
279 by NASA through a grant from the Space Telescope Science Institute, which is operated by the
280 Association of Universities for Research in Astronomy, Inc., under NASA contract NAS5-
281 26555. Daniel Toledo, Patrick Irwin and Nicholas Teanby acknowledge the support of the UK
282 Science and Technology Facilities Council. Glenn Orton acknowledges support from the
283 National Aeronautics and Space Administration that were distributed to the Jet Propulsion
284 Laboratory, California Institute of Technology. Telescope data are publicly available in ESO
285 repository (http://archive.eso.org/eso/eso_archive_main.html), and the reduced data and fits are
286 available from the authors.

287

288 **References**

- 289 Borysow, A., & Frommhold, L. (1987). Collision-induced Rototranslational Absorption Spectra
290 of N₂--N₂ Pairs for Temperatures from 50 to 300 K: Erratum. *The Astrophysical Journal*,
291 320, 437. <https://doi.org/10.1086/165558>
- 292 Borysow, A., & Frommhold, L. (1989). Collision-induced infrared spectra of H₂-He pairs at
293 temperatures from 18 to 7000 K. II - Overtone and hot bands. *The Astrophysical Journal*,
294 341, 549. <https://doi.org/10.1086/167515>
- 295 Borysow, A., Borysow, J., & Fu, Y. (2000). Semi-empirical model of collision-induced
296 absorption spectra of H₂-H₂ complexes in the second overtone band of hydrogen at
297 temperatures from 50 to 500 K. *Icarus*, 145(2), 601–608.
298 <https://doi.org/10.1006/icar.2000.6384>
- 299 Campargue, A., Wang, L., Mondelain, D., Kass, S., Bézard, B., Lellouch, E., ... Drossart, P.
300 (2012). An empirical line list for methane in the 1.26-1.71 μm region for planetary
301 investigations (T=80-300K). Application to Titan. *Icarus*, 219(1), 110–128.
302 <https://doi.org/10.1016/j.icarus.2012.02.015>
- 303 Hammel, H. B., & Lockwood, G. W. (2007). Long-term atmospheric variability on Uranus and
304 Neptune. *Icarus*, 186(1), 291–301. <https://doi.org/10.1016/j.icarus.2006.08.027>
- 305 Hofstadter, M. D., & Butler, B. J. (2003). Seasonal change in the deep atmosphere of Uranus.
306 *Icarus*, 165(1), 168–180. [https://doi.org/10.1016/S0019-1035\(03\)00174-X](https://doi.org/10.1016/S0019-1035(03)00174-X)
- 307 Hueso, R., Juaristi, J., Legarreta, J., Sánchez-Lavega, A., Rojas, J. F., Erard, S., ... Le Sidaner, P.
308 (2018). The Planetary Virtual Observatory and Laboratory (PVOL) and its integration into
309 the Virtual European Solar and Planetary Access (VESPA). *Planetary and Space Science*,
310 150, 22–35. <https://doi.org/10.1016/j.pss.2017.03.014>
- 311 Irwin, P. G. J., Tice, D. S., Fletcher, L. N., Barstow, J. K., Teanby, N. A., Orton, G. S., & Davis,
312 G. R. (2015). Reanalysis of Uranus' cloud scattering properties from IRTF/SpEx
313 observations using a self-consistent scattering cloud retrieval scheme. *Icarus*, 250, 462–476.
314 <https://doi.org/10.1016/j.icarus.2014.12.020>
- 315 Irwin, P. G. J., Fletcher, L. N., Read, P. L., Tice, D., de Pater, I., Orton, G. S., ... Davis, G. R.
316 (2016). Spectral analysis of Uranus' 2014 bright storm with VLT/SINFONI. *Icarus*, 264,

- 317 72–89. <https://doi.org/10.1016/j.icarus.2015.09.010>
- 318 Irwin, P. G. J., Teanby, N. A., Davis, G. R., Fletcher, L. N., Orton, G. S., Calcutt, S. B., ...
 319 Hurley, J. (2012). Further seasonal changes in Uranus' cloud structure observed by Gemini-
 320 North and UKIRT. *Icarus*, 218(1), 47–55. <https://doi.org/10.1016/j.icarus.2011.12.001>
- 321 Irwin, P. G. J., de Bergh, C., Courtin, R., Bézard, B., Teanby, N. A., Davis, G. R., Hurley, J.
 322 (2012). The application of new methane line absorption data to Gemini-N/NIFS and
 323 KPNO/FTS observations of Uranus' near-infrared spectrum. *Icarus*, 220(2), 369–382.
 324 <https://doi.org/10.1016/j.icarus.2012.05.017>
- 325 Irwin, P. G. J., Teanby, N. A., de Kok, R., Fletcher, L. N., Howett, C. J. A., Tsang, C. C. C., ...
 326 Parrish, P. D. (2008). The NEMESIS planetary atmosphere radiative transfer and retrieval
 327 tool. *Journal of Quantitative Spectroscopy and Radiative Transfer*, 109(6), 1136–1150.
 328 <https://doi.org/10.1016/j.jqsrt.2007.11.006>
- 329 Irwin, P. G. J., Wong, M. H., Simon, A. A., Orton, G. S., & Toledo, D. (2017). HST/WFC3
 330 observations of Uranus' 2014 storm clouds and comparison with VLT/SINFONI and
 331 IRTF/Spex observations. *Icarus*, 288, 99–119. <https://doi.org/10.1016/j.icarus.2017.01.031>
- 332 Karkoschka, E. (2001). Uranus' apparent seasonal variability in 25 HST filters. *Icarus*, 151(1),
 333 84–92. <https://doi.org/10.1006/icar.2001.6599>
- 334 Karkoschka, E., & Tomasko, M. (2009). The haze and methane distributions on Uranus from
 335 HST-STIS spectroscopy. *Icarus*, 202(1), 287–309.
 336 <https://doi.org/10.1016/J.ICARUS.2009.02.010>
- 337 de Kleer, K., Luszcz-Cook, S., de Pater, I., Ádámkóvics, M., & Hammel, H. B. (2015). Clouds
 338 and aerosols on Uranus: Radiative transfer modeling of spatially-resolved near-infrared
 339 Keck spectra. *Icarus*, 256(Supplement C), 120–137.
 340 <https://doi.org/https://doi.org/10.1016/j.icarus.2015.04.021>
- 341 Lockwood, G. W., & Jerzykiewicz, M. (2006). Photometric variability of Uranus and Neptune,
 342 1950-2004. *Icarus*, 180(2), 442–452. <https://doi.org/10.1016/j.icarus.2005.09.009>
- 343 de Pater, I., Sromovsky, L. A., Fry, P. M., Hammel, H. B., Baranec, C., & Sayanagi, K. M.
 344 (2015). Record-breaking storm activity on Uranus in 2014. *Icarus*, 252, 121–128.
 345 <https://doi.org/10.1016/j.icarus.2014.12.037>
- 346 Pollack, J. B., K. Rages, S. K. Pope, M. G. Tomasko, P. N. Romani, and S. K. Atreya
 347 (1987). Nature of the stratospheric haze on Uranus: Evidence for condensed
 348 hydrocarbons. *J. Geophys. Res.*, 92(A13), 15037–15065, doi:10.1029/JA092iA13p15037.
- 349 Rages, K. A., Hammel, H. B., & Friedson, A. J. (2004). Evidence for temporal change at Uranus'
 350 south pole. *Icarus*, 172(2), 548–554. <https://doi.org/10.1016/j.icarus.2004.07.009>
- 351 Sheik-Bahae, M., (2005). Nonlinear Optics Basics. KramersKronig Relations in Nonlinear
 352 Optics. In Robert D. Guenther. *Encyclopedia of Modern Optics*. Amsterdam: Academic
 353 Press.

- 354 Sromovsky, L. A., & Fry, P. M. (2007). Spatially resolved cloud structure on Uranus:
355 Implications of near-IR adaptive optics imaging. *Icarus*, *192*(2), 527–557.
356 <https://doi.org/10.1016/j.icarus.2007.07.017>
- 357 Sromovsky, L. A., Fry, P. M., & Kim, J. H. (2011). Methane on Uranus: The case for a compact
358 CH₄ cloud layer at low latitudes and a severe CH₄ depletion at high-latitudes based on re-
359 analysis of Voyager occultation measurements and STIS spectroscopy. *Icarus*, *215*(1), 292–
360 312. <https://doi.org/10.1016/j.icarus.2011.06.024>
- 361 Sromovsky, L. A., de Pater, I., Fry, P. M., Hammel, H. B., & Marcus, P. (2015). High S/N Keck
362 and Gemini AO imaging of Uranus during 2012-2014: New cloud patterns, increasing
363 activity, and improved wind measurements. <https://doi.org/10.1016/j.icarus.2015.05.029>
- 364 Sromovsky, L. A., Karkoschka, E., Fry, P. M., Hammel, H. B., de Pater, I., & Rages, K. (2014).
365 Methane depletion in both polar regions of Uranus inferred from HST/STIS and
366 Keck/NIRC2 observations. *Icarus*, *238*, 137–155.
367 <https://doi.org/10.1016/j.icarus.2014.05.016>
- 368 Tice, D. S., Irwin, P. G. J., Fletcher, L. N., Teanby, N. A., Hurley, J., Orton, G. S., & Davis, G.
369 R. (2013). Uranus' cloud particle properties and latitudinal methane variation from IRTF
370 SpeX observations. *Icarus*, *223*(2), 684–698. <https://doi.org/10.1016/j.icarus.2013.01.006>
- 371 Zheng, C., & Borysow, A. (1995). Modeling of collision-induced infrared absorption spectra of
372 H₂ pairs in the first overtone band at temperatures from 20 to 500 K. *Icarus*, *113*(1), 84–90.
373 <https://doi.org/10.1006/icar.1995.1006>
- 374
- 375